Proceedings of the Canadian Society for Mechanical Engineering International Congress
32nd Annual Conference of the Computational Fluid Dynamics Society of Canada
Canadian Society of Rheology Symposium
CSME/CFDSC/CSR 2025
May 25–28, 2025, Montréal, Québec, Canada

Effect of Laser Powder Bed Fusion Process Parameters on Microstructure and Coefficient of Thermal Expansion of Al6061

Faezeh Hosseini*, Asad Asad, Mostafa Yakout

Department of Mechanical Engineering, University of Alberta, Edmonton, Alberta, T6G 1H9, Canada
*fhossei1@ualberta.ca

***Abstract*—**
High-performance aluminum (Al) alloys, including the 6xxx and 7xxx series, are considered promising materials for energy, aerospace, automotive, and defense applications. In this work, the laser powder bed fusion (L-PBF) technique was employed to fabricate Al6061. An optimized processing window for L-PBF was established to fabricate Al6061 with relative densities exceeding 99%, using a laser power range of 200–250 W, a scanning speed of 1000 mm/s, and a hatch spacing of 140 μm. This process resulted in complete melting within the energy density range of 44–50 J/mm^3. Additionally, thermal expansion and average linear coefficient of thermal expansion (CTE) analyses revealed that parts produced at energy densities below 44.64–50 J/mm^3 exhibited lower CTE, likely due to void formation in the lack of fusion mode. Similarly, higher energy densities (69.44 and 104.16 J/mm^3) also caused a decrease in CTE, attributed to phase transformations and keyhole formation.

***Keywords-component*—additive manufacturing; laser powder bed fusion (L-PBF); Al6061; melting regimes; coefficient of thermal expansion (CTE)**

I. INTRODUCTION

High-performance aluminum (Al) alloys, including the 6xxx and 7xxx series, are known for their high strength, low density, and enhanced corrosion resistance, making them promising materials for energy, aerospace, automotive, and defense applications [1], [2].

Laser Powder Bed Fusion (L-PBF) is a widely used metal additive manufacturing (AM) process that fabricates parts by selectively melting predefined layers of metal powders [3]. It offers distinct advantages, such as the formation of non-equilibrium solidification microstructures due to the rapid heating, melting, cooling, and solidification cycles in L-PBF [4], [5]. The high cooling rates associated with this process promote increased solute solid solubility, finer grain sizes, and reduced element segregation compared to conventional processing methods [6]. As a result, L-PBF enables tailoring the microstructure and mechanical properties of Al alloys.

However, L-PBF of Al alloys, such as Al6061, results in defects such as solidification cracking and porosity [7]. These issues arise from physical properties, including low laser beam absorptivity, tenacious oxide films, low boiling point elements, high thermal conductivity, high coefficient of thermal expansion, relatively wide solidification temperature ranges, and significant solidification shrinkage [8]. Therefore, L-PBF process parameters, including laser power, scanning speed, hatch spacing and layer thickness must be optimized to fully melt the Al alloy powder [9]. One of the commonly used metrics to optimize these process parameters is the laser energy density (E_v, J/mm^3), calculated as [10]:

$$E_v = \frac{P}{v \cdot t \cdot h} \tag{1}$$

where P is the laser power (W), v is the scan speed (mm/s), t is the layer thickness (mm), and h is the hatch spacing (mm). Maamoun et al. [11] observed that defect size and distribution in L-PBF-fabricated Al6061 vary with processing conditions, leading to solidification cracking within the microstructure. An optimized energy density of 52.6 J/mm^3 was identified, resulting in the smallest microcracks.

Variations in process parameters can lead to different melting modes and defect formations in laser-based metal AM. The energy density plays a crucial role in determining these outcomes. An optimized laser energy density ensures complete powder melting, facilitating sufficient melt pool overlap and reducing defect formation [12]. Insufficient energy input results in lack of fusion defects, characterized by irregular pores and unmelted powder particles due to inadequate thermal input for bonding with the previously deposited layer [13]. Conversely, excessive energy input at high power and low

This work was partially supported by funding from the Natural Science and Engineering Research Council of Canada (NSERC) Discovery Grant (RGPIN-2023-04004).

scanning speeds, induces the keyhole mode. This leads to an increased melt pool depth-to-width ratio, promoting the formation of vapor cavities and causing microsegregation of alloying elements, contributing to defect generation [14].

Attempts have been made to fabricate Al6061 using L-PBF through approaches such as optimizing process parameters and introducing alloying elements to minimize solidification cracking. Uddin et al. [15] successfully produced crack-free Al6061 samples using the L-PBF process by preheating the platform to 500 °C and applying process parameters of 400 W and 1400 mm/s. The success was attributed to the high-temperature preheating, which eliminated melt-pool banding and facilitated the nucleation of large non-coherent precipitates in the columnar grain boundaries. Chen et al. [16] demonstrated that incorporating yttria-stabilized zirconia (YSZ) into Al6061 eliminated cracking during the L-PBF process. This was attributed to the substantial reduction in grain size and the formation of fine equiaxed grains along the melt pool boundaries, which prevented crack propagation along the grain boundaries. Additionally, Mehta et al. [17] studied the impact of adding 1 wt% Zr to Al6061 and found that it not only reduced crack formation but also minimized internal porosity due to significant grain refinement, thus enhancing the material's resistance to hot cracking.

However, the literature lacks information on the influence of L-PBF process parameters on the CTE of Al6061, which is critical as changes in thermal expansion can affect crack formation [18]. The CTE is a key thermophysical property, particularly in L-PBF, where high cooling rates and rapid thermal cycles can cause thermal heterogeneity [19], [20]. This leads to residual stresses, which, if not controlled, can contribute to defects like cracking during fabrication [20]. Therefore, understanding the impact of L-PBF parameters on the CTE of Al6061 is essential for optimizing part quality and minimizing defects. The columnar grain structure typically observed in L-PBF-fabricated samples could result in a higher CTE compared to conventionally manufactured Al alloys with an equiaxed microstructure [21]. Additionally, variations in energy density are expected to influence defect formation and phase transformations, further affecting the CTE.

This study aims at investigating the effect of process parameters including laser power, scanning speed and hatch spacing on the density, microstructure, and thermal properties of L-PBF-fabricated Al6061, focusing on identifying the melting modes for different energy densities.

II. Materials and Methods

A. Powder Feedstock

In this study, gas-atomized Al6061 powder, supplied by Valimet Inc. (Stockton, CA, USA), was used as the feedstock material. The powder size distribution (PSD) was measured using Malvern Morphologi G3 (Malvern Panalytical, UK) automated particle size analyzer. Powder morphology was analyzed using a field-emission scanning electron microscope (FE SEM, Zeiss Sigma FESEM, Germany).

B. L-PBF Process Parameters

Samples were fabricated using an EOS M290 L-PBF (EOS GmbH, Krailling, Germany) machine with a 400 W Yb-fiber laser and a 100 μm laser spot size. The build plate was preheated to 180 °C, and each layer was rotated by 67°, with a constant thickness of 0.04 mm. A design of experiment (DOE) based on the L9 orthogonal array of the Taguchi method was used to study three factors—laser power (P), scanning speed (V), and hatch spacing (h)—each at three levels, as shown in Table I. The levels were determined from open literature [16], [17], [22]–[24], resulting in 9 experimental runs and laser energy densities ranging from 25.51 to 104.06 J/mm^3.

TABLE. I
L-PBF PROCESS PARAMETERS USED IN THIS STUDY

Laser Power (W)	Scanning Speed (mm/s)	Hatch Spacing (mm)	Energy Density (J/mm^3)
150	600	0.14	44.64
150	1000	0.12	31.25
150	1400	0.1	26.78
200	600	0.12	69.44
200	1000	0.1	50.00
200	1400	0.14	25.51
250	600	0.1	104.16
250	1000	0.14	44.64*
250	1400	0.12	37.20

*Indicates higher laser power for the same energy density.

C. Microstructure Characterization

The as-built samples were sectioned perpendicular to the build direction. The specimens were first ground using 600- and 1200-grit SiC paper and then polished sequentially with diamond suspensions of 9 μm, 6 μm, 3 μm, and 1 μm. Microstructural analysis was performed using a field-emission scanning electron microscope (FE SEM, Zeiss Sigma, Germany) equipped with electron-backscattered diffraction (EBSD). For EBSD, the sample surfaces were mirror-polished using ion beam polishing with a plasma focused ion beam (PFIB, Helios Hydra, Thermo Fisher, USA). A 500 μm diameter area was polished with a 30 kV, 60 nA Xe beam using spin milling. Three EBSD maps, each with a 400 $\times$ 300 μm^2 area and a step size of 0.75 μm, were acquired at 15 kV, using a 60 μm aperture and high current mode. Post-processing was conducted using Channel 5 software. Additionally, X-ray diffraction (XRD, Ultima IV, Rigaku, Japan) was performed to identify the phases and intermetallics present in the samples. The polished samples were exposed to Cu-Kα radiation ($\lambda = 1.54056$ Å) using scanning speeds of 2°/min.

D. Density

Density measurements were conducted on all samples to evaluate their porosity using the Archimedes principle, in accordance with ASTM B962-23 [25]. The measured densities were compared to the reference value of 2.7 g/cm^3 for bulk Al6061 and presented as relative densities [26]. Each sample's density was calculated using Equation (2):

$$\rho = \rho_w \times \left(\frac{W_1}{W_1 - W_2} \right)$$

where W_1 is the weight of the dry sample, W_2 is the weight of the sample when immersed, and ρ_w is the density of water.

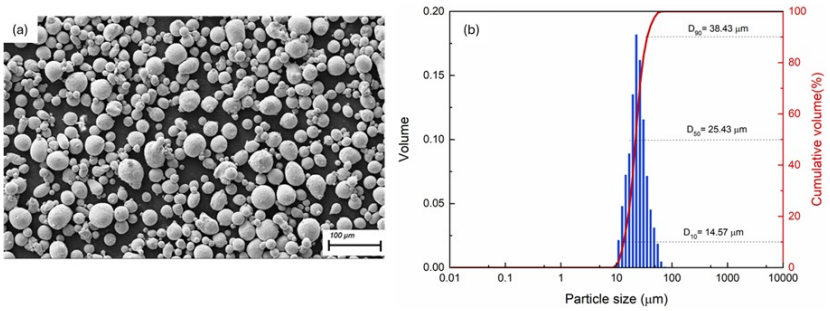

Figure. 1. Morphology of (a) virgin, (b) powder size distribution of Al6061 powder [27].

E. CTE Analysis

CTE samples were fabricated following the ASTM E831-14 standard size [28] and a NETZSCH DIL 402 dilatometer (NETZSCH-Gerätebau GmbH, Germany) was used to measure the apparent CTE for each sample. The tests were conducted between 25°C and 450°C with a heating rate of 0.1 °C/s, followed by cooling to room temperature. The apparent CTE, α, expressed in ($10^{-6}\,^{\circ}\mathrm{C}^{-1}$), and the apparent thermal expansion, ϵ_T, were calculated using equation 2 [29]:

$$\alpha = \left(\frac{\Delta L}{L_0 \times \Delta T}\right) = \left(\frac{\epsilon_T}{\Delta T}\right), \text{ where } \epsilon_T = \left(\frac{\Delta L}{L_0}\right) \quad (2)$$

Where, ΔL is the change in length in (μm), ΔT is the temperature difference over which ΔL is measured in (°C), L_0 is the initial length in (m).

III. Results and Discussion

A. Powder Characterization

The morphology of the Al6061 powders is shown in Figure 1a. The virgin powder consists of nearly regular spherical particles. Particle size distribution ranged from 9 to 40 μm. The powder diameter at three cumulative volumes of particles of 10%, 50%, and 90% are D_{10} = 14.57 μm, D_{50} = 25.43 μm, D_{90} = 38.43 μm, as shown in Figure 1b. The nominal PSD values provided by the supplier are D10 = 24–30 μm, D50 = 40–47 μm, and D90 = 60–68 μm.

B. Crystallographic Characterization

Figure 2 presents the XRD patterns of the Al6061 alloy fabricated via L-PBF at different energy densities of 25.51 J/mm^3, 50 J/mm^3, and 104.16 J/mm^3. The XRD results primarily show peaks associated with the α-Al (FCC) phase. The spectrum also reveals a strong grain orientation along the (200) direction, indicating a noticeable texture formation in this direction. In L-PBF, the repeated melting and solidification cycles generate a steep thermal gradient, predominantly along the build direction. In cubic metals, grain growth is typically favored along the $\langle 100 \rangle$ crystallographic direction due to its lower packing efficiency. Consequently, most grains align with the $\langle 100 \rangle$ direction [17]. As the energy density increased to 104.16 J/mm^3, additional phases, including Mg_2Si and $AlMg_4Si_3$, appeared in the XRD patterns. This is likely due to the higher temperatures associated with the increased energy density, which provided the necessary thermal energy for the precipitation of these phases [17].

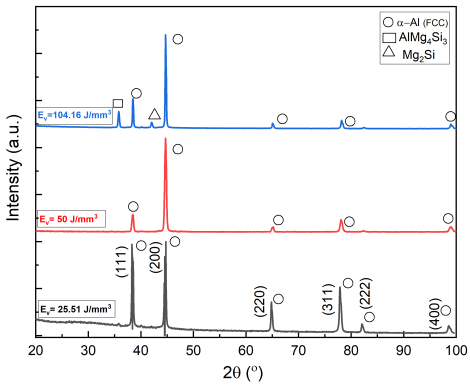

Figure. 2. X-ray diffraction (XRD) patterns of As-built Al6061 samples fabricated at energy densities of 25.51 J/mm^3, 50 J/mm^3, and 104.16 J/mm^3 [27].

C. Microstructure Characterization

The XY cross-sectional micrographs of the L-PBF samples fabricated at different energy densities are shown in Figure 3. Based on the defect morphology, the processing parameter map can be categorized into lack of fusion, stable, and keyhole modes. At lower energy densities (red box), which correspond to relatively lower laser power and higher scanning speed, lack of fusion pores with visible unmelted powder around them were observed. These defects likely resulted from insufficient energy applied to fully melt the powder, leading to poor bonding between powder layers [30]. In contrast, keyhole pores appeared in samples fabricated at higher power and lower speed, corresponding to higher energy densities (blue box). These pores formed due to excessive laser penetration into the deposited layers, creating an overly deep melt pool [13]. These defects were reduced by using an energy density range of 44–50 J/mm^3 (yellow box). The stable melting mode indicates that a proper energy input is crucial for fully melting the material, resulting in a dense part.

The melting mode was evaluated using Thermo-Calc's Additive Manufacturing Module (2024b) with the TCAl9 database. A steady-state simulation using a calibrated Gaussian

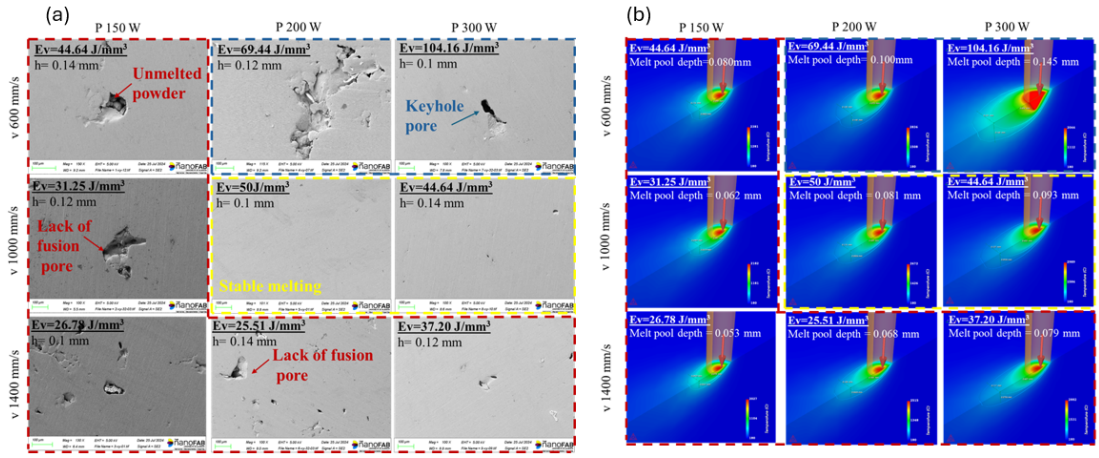

Figure. 3. (a) SEM micrographs of the as-built Al6061 samples [27], and (b) predicted melt-pool dimensions under different combinations of process parameters.

heat source predicted melt pool depths for each set of process parameters [31], shown in Figure 3b. At low energy densities (25.51–44.64 J/mm^3), the simulated melt pools were shallow, characteristic of the lack of fusion regime that can lead to incomplete bonding and porosity. Increasing the energy density (69.44 and 104.16 J/mm^3) produced deeper melt pools prone to keyhole porosity [14]. Within the optimized window (44.64–50 J/mm^3), melt-pool dimensions promote complete fusion, characteristic of a stable melting mode that correlates with the highest relative density (99%) and minimal internal defects. These predictions are consistent with the melting modes observed in the SEM images (Figure 3a).

The grain growth and crystallographic orientation of the Al6061 samples fabricated at energy densities of 31.25 J/mm^3, 44.64 J/mm^3, and 104.16 J/mm^3 were investigated through EBSD characterization, which indicates texture randomization for all three samples. The band contrast (BC) images in Figure 4b reveal the presence of cracks and porosities in all three samples. The samples fabricated at 31.25 J/mm^3 and 104.6 J/mm^3 exhibited a higher number of defects, which is consistent with the SEM observations shown in Figure 3. The grain size distribution for the sample fabricated at 31.25 J/mm^3 ranged from 0.5 μm to 121.5 μm, with an average size of 61 μm. For the sample at 44.64 J/mm^3, the grain size ranged from 0.5 μm to 129.5 μm, with an average of 65 μm. Finally, for the sample at 104.6 J/mm^3, the grain size ranged from 0.5 μm to 103.5 μm, with an average size of 52 μm.

D. Part Density

Figure 5 shows the relative density as a function of laser energy density. Similarly, as observed in Figure 3, samples with both low and high energy densities, corresponding to lack of fusion and keyhole modes, exhibited poor relative densities due to significant internal defects. At low energy densities, unmelted powder particles were present, while at very high energy densities, microsegregation and vaporization of low-melting-point elements occurred, leading to a reduction in part

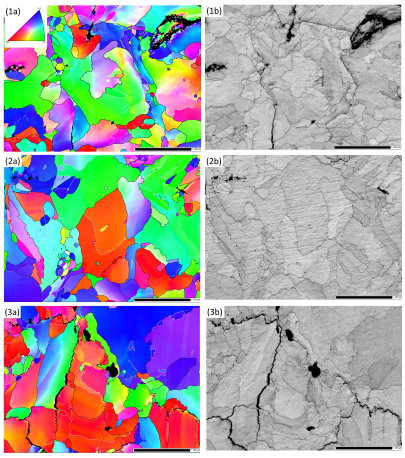

Figure. 4. (a) Band contrast (BC), and (b) EBSD maps of as-built Al6061 at energy densities of (1) 31.25 J/mm^3, (2) 44.64 J/mm^3, and (3) 104.16 J/mm^3 [27].

density [32]. Among the evaluated parameters, the optimal value was 44.64 J/mm^3, with a relative density of 99%.

E. Coefficient of Thermal Expansion

Figures 6a and b show the thermal expansion and average linear CTE for Al6061 parts produced at different laser energy densities. The L-PBF parts exhibited higher average CTE compared to the conventionally manufactured Al alloys, with values of $30 \times 10^{-6}\,°C^{-1}$ compared to $24 \times 10^{-6}\,°C^{-1}$. This is consistent with literature suggesting that the columnar microstructure results in higher CTE values [33], [34]. It was observed that parts produced at laser energy densities below 44.64–50 J/mm^3 exhibited lower thermal expansion. This is likely due to void formation in the lack of fusion mode at lower energy densities [35]. Increasing the laser energy density to 69.44 and 104.16 J/mm^3 also caused a decrease in CTE, which can be attributed to phase transformations and keyhole formation at energy densities above the optimized range [29].

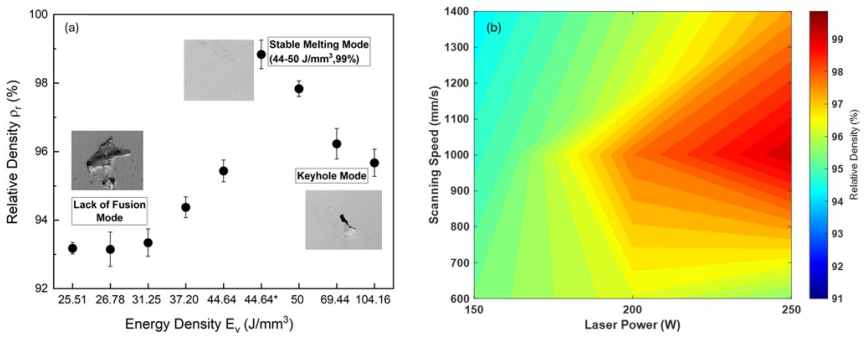

Figure. 5. Relative density of L-PBF parts as a function of (a) laser energy density, and (b) under different combinations of laser power and scanning speed.

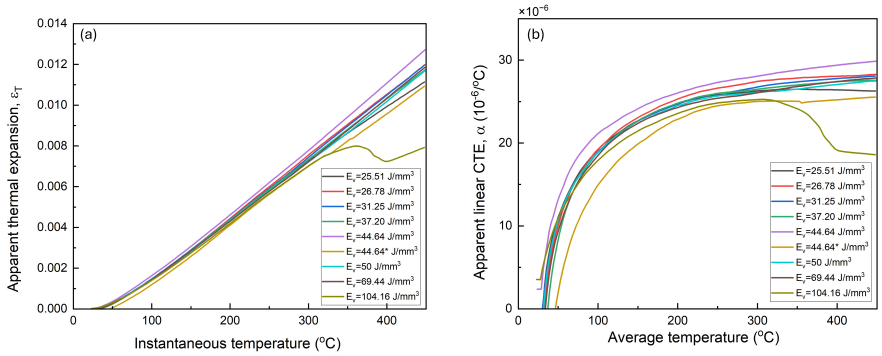

Figure. 6. (a) Apparent linear thermal expansion, and (b) apparent linear coefficient of thermal expansion of Al6061 parts manufactured at different laser energy densities.

The decrease in CTE at 104.16 J/mm^3 is particularly notable and may be attributed to the formation of additional phases, such as Mg_2Si and $AlMg_4Si_3$, as observed in the XRD data shown in Figure 2. These phase transformations can affect the material's thermal expansion behavior by altering its microstructure [36]. The lowest CTE was observed at 104.16 J/mm³; however, this will still be considered a defective sample because it falls within the keyhole melting regime [37]. This energy density also corresponds to a finer grain structure, and this observation aligns with the findings of Su et al. [37], which indicate that in L-PBF of Al–Si alloys, CTE decreases with decreasing grain size.

IV. Conclusion

This study explored the effects of L-PBF process parameters on Al6061. Achieving crack-free fabrication of Al6061 has been challenging; therefore, optimizing process parameters is essential to produce high-quality parts. Our findings indicate that controlling the energy density is crucial for optimizing the microstructure and properties. The reduction of defects in Al6061 using L-PBF was demonstrated by optimizing energy density. This was achieved by fine-tuning laser power, scanning speed, and hatch spacing to identify an optimal energy density range of 44–50 J/mm^3 which significantly reduced defects and improved part density. Additionally, the CTE results show that porosity, including keyhole and lack of fusion porosity, as well as phase transformations at higher energy densities, lower the CTE. In conclusion, this work demonstrates that adjusting processing conditions—specifically laser power, scanning speed, and hatch spacing—can effectively eliminate defects in L-PBF-fabricated parts. The high CTE of Al6061 plays a significant role in the melting and solidification process. A lower energy density can lead to increased heat dissipation and a faster solidification rate, which, combined with the material's higher reflectivity and CTE, makes it more difficult to fully melt the powder layer, potentially resulting in solidification cracking [38]. Understanding the role of CTE in determining the melting modes and solidification regimes is critical to further optimizing processing parameters to reduce defects. Future work will focus on further fine-tuning these processing parameters to optimize L-PBF fabrication of Al6061. We aim to explore these refined parameters for their potential in industrial applications, ensuring the successful processing of Al6061 for various practical uses.

Acknowledgment

This work was partially supported by funding from the Natural Science and Engineering Research Council of Canada (NSERC) Discovery Grant (RGPIN-2023-04004). The authors thank the Additive Metal Manufacturing Inc. (Ontario) team for helping with the printing process. The authors also thank Cass (Haoyang) Li, Project Manager in the Department of Mechanical Engineering at the University of Alberta, for helping with the powder analysis.

REFERENCES

[1] S. Dixit and S. Liu, "Laser additive manufacturing of high-strength aluminum alloys: challenges and strategies," *J. Manuf. Mater. Process.*, vol. 6, no. 6, p. 156, 2022.

[2] T.-S. Liu, P. Chen, F. Qiu, H.-Y. Yang, N. T. Y. Jin, Y. Chew, D. Wang, R. Li, Q.-C. Jiang, and C. Tan, "Review on laser directed energy deposited aluminum alloys," *Int. J. Extreme Manuf.*, vol. 6, no. 2, p. 022004, 2024.

[3] S. Sun, M. Brandt, and M. J. L. A. M. Easton, "Powder bed fusion processes: An overview," in *Laser Additive Manufacturing*, Elsevier, 2017, pp. 55–77.

[4] Z. Dong, C. Han, Y. Zhao, J. Huang, C. Ling, G. Hu, Y. Wang, D. Wang, C. Song, and Y. Yang, "Role of heterogeneous microstructure and deformation behavior in achieving superior strength-ductility synergy in zinc fabricated via laser powder bed fusion," *Int. J. Extreme Manuf.*, vol. 6, no. 4, p. 045003, 2024.

[5] A. Martucci, A. Aversa, and M. Lombardi, "Ongoing challenges of laser-based powder bed fusion processing of Al alloys and potential solutions from the literature—A review," *Mater.*, vol. 16, no. 3, p. 1084, 2023.

[6] T. Mukherjee, J. W. Elmer, H. L. Wei, T. J. Lienert, W. Zhang, S. Kou, and T. DebRoy, "Control of grain structure, phases, and defects in additive manufacturing of high-performance metallic components," *Prog. Mater. Sci.*, vol. 138, p. 101153, 2023.

[7] H. Wang, X. Wang, J. Zou, H. Zhou, Q. Zheng, J. Bi, M. D. Starostenkov, G. Dong, and C. Tan, "Recent progress on the control strategies of microstructure and mechanical properties of LPBF-printed aluminum alloys," *Int. J. Adv. Manuf. Technol.*, vol. 134, no. 9, pp. 4015–4039, 2024.

[8] E. O. Olakanmi, R. F. Cochrane, and K. W. Dalgarno, "A review on selective laser sintering/melting (SLS/SLM) of aluminium alloy powders: Processing, microstructure, and properties," *Prog. Mater. Sci.*, vol. 74, pp. 401–477, 2015.

[9] L. Scime and J. Beuth, "Melt pool geometry and morphology variability for the Inconel 718 alloy in a laser powder bed fusion additive manufacturing process," *Addit. Manuf.*, vol. 29, p. 100830, 2019.

[10] N. T. Aboulkhair, M. Simonelli, L. Parry, I. Ashcroft, C. Tuck, and R. Hague, "3D printing of Aluminium alloys: Additive Manufacturing of Aluminium alloys using selective laser melting," *Prog. Mater. Sci.*, vol. 106, p. 100578, 2019.

[11] A. H. Maamoun, Y. F. Xue, M. A. Elbestawi, and S. C. Veldhuis, "The effect of selective laser melting process parameters on the microstructure and mechanical properties of Al6061 and AlSi10Mg alloys," *Mater.*, vol. 12, no. 1, p. 12, 2018.

[12] A. Mostafaei, C. Zhao, Y. He, S. R. Ghiaasiaan, B. Shi, S. Shao, N. Shamsaei, Z. Wu, N. Kouraytem, T. Sun, and others, "Defects and anomalies in powder bed fusion metal additive manufacturing," *Curr. Opin. Solid State Mater. Sci.*, vol. 26, no. 2, p. 100974, 2022.

[13] M. Yakout, M. A. Elbestawi, and S. C. Veldhuis, "A study of thermal expansion coefficients and microstructure during selective laser melting of Invar 36 and stainless steel 316L," *Addit. Manuf.*, vol. 24, pp. 405–418, 2018.

[14] P. Promoppatum, S.-C. Yao, P. C. Pistorius, and A. D. Rollett, "A comprehensive comparison of the analytical and numerical prediction of the thermal history and solidification microstructure of Inconel 718 products made by laser powder-bed fusion," *Eng.*, vol. 3, no. 5, pp. 685–694, 2017.

[15] S. Z. Uddin, L. E. Murr, C. A. Terrazas, P. Morton, D. A. Roberson, and R. B. Wicker, "Processing and characterization of crack-free aluminum 6061 using high-temperature heating in laser powder bed fusion additive manufacturing," *Addit. Manuf.*, vol. 22, pp. 405–415, 2018.

[16] H. H. Chen, Y. L. Lo, Y. Y. Hsu, and K. L. Lai, "Systematic optimization of L-PBF processing parameters for Al alloy 6061 with YSZ nanoparticles," *Opt. Laser Technol.*, vol. 167, p. 109676, 2023.

[17] A. Mehta, L. Zhou, T. Huynh, S. Park, H. Hyer, S. Song, Y. Bai, D. D. Imholte, N. E. Woolstenhulme, D. M. Wachs, and others, "Additive manufacturing and mechanical properties of the dense and crack-free Zr-modified aluminum alloy 6061 fabricated by the laser-powder bed fusion," *Addit. Manuf.*, vol. 41, p. 101966, 2021.

[18] B. A. Fulcher, D. K. Leigh, and T. J. Watt, "Comparison of AlSi10Mg and Al 6061 processed through DMLS," 2014, University of Texas at Austin.

[19] J. D. James, J. A. Spittle, S. G. R. Brown, and R. W. Evans, "A review of measurement techniques for the thermal expansion coefficient of metals and alloys at elevated temperatures," *Measurement Science and Technology*, vol. 12, no. 3, p. R1, 2001.

[20] L. Yuan, H. Ji, and D. Shan, "Effect of cohesive energy on thermal expansion behavior of T6 tempered 7A09 aluminum alloy," *J. Alloys Compd.*, vol. 513, pp. 546–551, 2012.

[21] N. J. Harrison, I. Todd, and K. Mumtaz, "Thermal expansion coefficients in Invar processed by selective laser melting," *J. Mater. Sci.*, vol. 52, pp. 10517–10525, 2017.

[22] A. Sonawane, G. Roux, J.-J. Blandin, A. Despres, and G. Martin, "Cracking mechanism and its sensitivity to processing conditions during laser powder bed fusion of a structural aluminum alloy," *Materialia*, vol. 15, p. 100976, 2021.

[23] M. Opprecht, J.-P. Garandet, G. Roux, C. Flament, and M. Soulier, "A solution to the hot cracking problem for aluminium alloys manufactured by laser beam melting," *Acta Mater.*, vol. 197, pp. 40–53, 2020.

[24] G. Melek, P. Eloi, J.-J. Blandin, C. Pascal, P. Donnadieu, F. De Geuser, P. Lhuissier, C. Desrayaud, and G. Martin, "Optimization of the strength vs. conductivity trade-off in an aluminium alloy designed for laser powder bed fusion," *Mater. Sci. Eng. A*, vol. 858, p. 144139, 2022.

[25] *ASTM B962-23*; ASTM International Committee B09 on Metal Powders and Metal Powder Products, "Standard Test Methods for Density of Compacted or Sintered Powder Metallurgy (PM) Products Using Archimedes' Principle," ASTM International, West Conshohocken, PA, USA, 2023.

[26] A. H. Committee, "Properties of Wrought Aluminum and Aluminum Alloys, Properties and Selection: Nonferrous Alloys and Special-Purpose Materials," *ASM Handb.*, vol. 2, pp. 62–122, 1990.

[27] F. Hosseini, A. Asad, M. Yakout, "Microstructure Characterization and Mechanical Properties of Al6061 Alloy Fabricated by Laser Powder Bed Fusion," *J. Manuf. Mater. Process.*, vol. 8, p. 288, 2024. https://doi.org/10.3390/jmmp8060288

[28] ASTM International, "Standard test method for linear thermal expansion of solid materials by thermomechanical analysis," ASTM E831-14, 2014.

[29] M. Yakout, M. A. Elbestawi, and S. C. Veldhuis, "A study of the relationship between thermal expansion and residual stresses in selective laser melting of Ti-6Al-4V," *Journal of Manufacturing Processes*, vol. 52, pp. 181–192, 2020.

[30] X. Yang, Y. Li, and B. Li, "Formation mechanisms of lack of fusion and keyhole-induced pore defects in laser powder bed fusion process: A numerical study," *Int. J. Therm. Sci.*, vol. 188, p. 108221, 2023.

[31] A. Fardan, A. Fazi, R. L. Peng, T. Mishurova, M. Thuvander, G. Bruno, H. Brodin, and E. Hryha, "Fine-tuning melt pools and microstructures: Taming cracks in powder bed fusion—laser beam of a non-weldable Ni-base superalloy," *Materialia*, vol. 34, p. 102059, 2024.

[32] M. Yakout, M. A. Elbestawi, and S. C. Veldhuis, "Density and mechanical properties in selective laser melting of Invar 36 and stainless steel 316L," *J. Mater. Process. Technol.*, vol. 266, pp. 397–420, 2019.

[33] C. R. Kumar, R. R. Malarvannan, and V. JaiGanesh, "Role of SiC on mechanical, tribological and thermal expansion characteristics of B4C/Talc-reinforced Al-6061 hybrid composite," *Silicon*, vol. 12, no. 6, pp. 1491–1500, 2020.

[34] G. B. Veeresh Kumar, R. Pramod, R. H. Kiran Reddy, P. Ramu, B. Kunaal Kumar, P. Madhukar, M. Chavali, F. Mohammad, and S. K. Khiste, "Investigation of the tribological characteristics of aluminum 6061-reinforced titanium carbide metal matrix composites," *Nanomaterials*, vol. 11, no. 11, p. 3039, 2021.

[35] D. Guillen, S. Wahlquist, and A. Ali, "Critical review of LPBF metal print defects detection: roles of selective sensing technology," *Appl. Sci.*, vol. 14, no. 15, p. 6718, 2024.

[36] C. Jaramillo-Isaza, O. F. Higuera-Cobos, J. A. Taborda-Ríos, O. E. Lopez-Botello, and P. Zambrano-Robledo, "Correlation of energy density and manufacturing variables of AA6061 through laser powder bed fusion and its effect on the densification mechanism," *Metals*, vol. 13, no. 11, p. 1904, 2023.

[37] B. Su, H. Chao, Y. Jin, G. Cui, M. Zhong, B. Wang, L. Luo, L. Wang, Y. Su, H. Huang, *et al.*, "Influence of heat treatment on microstructure and thermo-physical properties of Al-50wt% Si alloy fabricated by selective laser melting," *Journal of Materials Research and Technology*, vol. 30, pp. 4542–4551, 2024.

[38] A. H. Maamoun, Y. F. Xue, M. A. Elbestawi, and S. C. Veldhuis, "Effect of selective laser melting process parameters on the quality of Al alloy parts: Powder characterization, density, surface roughness, and dimensional accuracy," *Mater.*, vol. 11, no. 12, p. 2343, 2018.